



Estimating orientation of optically trapped, near vertical, microsphere dimers using central moments and off-focus imaging

ALLAN RAUDSEPP,^{1,*} GEOFFREY B. JAMESON,^{1,2} AND MARTIN A. K. WILLIAMS^{1,2}

¹School of Fundamental Sciences, Massey University, Palmerston North 4472, New Zealand

²MacDiarmid Institute, Victoria University of Wellington, Wellington, New Zealand

*Corresponding author: A.Raudsepp@massey.ac.nz

Received 22 October 2021; revised 12 December 2021; accepted 14 December 2021; posted 15 December 2021; published 10 January 2022

Near vertical optically trapped dimers, composed of pairs of microspheres, and constructed *in situ*, were imaged in bright-field in flow and at rest, and with displacement Δz from the transverse x - y imaging plane of an inverted microscope. Image first central moments μ_{01} were measured, and their dependence on the imposed flow velocity of the surrounding fluid was calculated. This dependence was related to the at-rest restricted diffusion statistics. It was assumed that, for small perturbations, the torque T on the dimer was proportional to the velocity of flow v and resulting angular deflection $\Delta\theta$ so that $T \propto v \propto \Delta\theta$. Displacements Δz at which $v \propto \Delta\mu_{01} \propto \Delta\theta$, which are typically off focus, were examined in more detail; in this range, $\Delta\theta = b\Delta\mu_{01}$. The hydrodynamics of the dimer were modeled as that of a prolate ellipsoid, and the constant of proportionality b was determined by comparing the short-time mean-squared variation measured during diffusion to that predicted by the model calculation: $b^2\langle\Delta\mu_{01}^2(t)\rangle = \langle\Delta\theta^2(t)\rangle$. With b determined, the optical trap stiffness k_θ was determined from the long-time restricted diffusion of the dimer. The measured k_θ and $\Delta\theta$ can then be used to compute torque: $T = k_\theta\Delta\theta$, potentially enabling the near vertical optically trapped dimer to be used as a torque probe. © 2022 Optica Publishing Group

<https://doi.org/10.1364/AO.446610>

1. INTRODUCTION

In appropriate conditions, microspheres in suspension can spontaneously stick, producing a bead pair that has been called a dimer, dicolloid, or a dumb-bell. Unlike isolated microspheres, which are symmetric, these bead pairs are asymmetric, possessing a long axis and short axes. If the orientation of the long axis can be determined, the measured orientation can be used to investigate micro-particle rotational dynamics, which are not easy to study in isolated microspheres because of their symmetry.

Dimer orientation and dynamics have been studied using a number of techniques. In studies that make use of conventional microscopy, dimers are generally confined to the transverse imaging plane (x - y plane) either by proximity to a surface [1] or using other methods [2,3]. Orientation can be inferred from the asymmetry of the dimer's image. While this approach is straightforward, interpretation of the dimer's dynamics can be complicated by hydrodynamic interactions between the dimer and surface, if present. Holographic microscopy [4] and confocal microscopy [5] can be used to accurately determine the orientation in 3D, without the requirement to work within the range of hydrodynamic interactions of the surface. Clearly these approaches are more general; however, they do require additional hardware to facilitate measurement.

Optical tweezers use a highly focused laser to produce an optical trap, which, with appropriate hardware, can be used to manipulate micro-particles in suspension [6]. Focusing is usually achieved using a high numerical aperture (NA) microscope objective, which can also be used to image the trapped particle. The restoring force F produced by the trap (for standard gradient traps) is proportional to particle displacement Δy :

$$F = k_y \Delta y \quad (1)$$

for small displacements; if the trap stiffness k_y is known and Δy can be estimated, by image analysis, for example, the restoring force on the particle can be determined [6,7]. These measurements of the forces on micro-particles are an important application of optical tweezing. If two steerable traps are available, two-particle manipulations are possible, and a two-particle approach is the basis of common push- [8–12] and pull- [13–17] type experiments. If the particle Debye length is sufficiently small, particles may stick when pushed together, forming a dimer, and this can occur quite accidentally during push (or pull) experiments (often ending the experiment with those particles).

Optically trapped dimers formed in this way are observed to orient with their long axis vertically aligned with the longitudinal axis of a standard gradient trap (z direction). This observation appears to be in accordance with the prediction that the longest axis of dielectric ellipsoids will tend to align with the longitudinal axis [18]. This orientation largely hides the asymmetry observed in transverse studies, effectively concealing the relationship between image and orientation. In this work, we examine optically trapped dimers and demonstrate using a combination of flow and restricted diffusion measurements, along with hydrodynamic modeling, that variations in the dimer's bright-field image central moment are related to angular deflections of the dimer, and that this relationship depends on the dimer's displacement from the imaging plane. Once this relationship is understood, an angular trap stiffness k_θ can be estimated, enabling a calculation of the torque T on the dimer:

$$T = k_\theta \Delta\theta. \quad (2)$$

2. EXPERIMENTAL

Optical tweezing was carried out on an inverted microscope (Nikon Eclipse TE2000-U) equipped with holographic optical tweezers (Arryx). In this setup, light from a $\lambda = 1064$ nm NIR 2 W laser is reflected from a computer-controlled (Red Tweezers [19]) spatial light modulator (Boulder NLS phase only) and focused into the sample via a high NA water immersion objective (Nikon, NA = 1.2 magnification, 60 \times), and the sample imaged in bright-field using a high-speed camera (Andor Technology NEO) at 200 frames per second (FPS), unless noted otherwise. Dimers composed of $2a = 1250$ nm, $2a = 810$ nm, or $2a = 2120$ nm diameter bead pairs (Spherotech) were examined in standard cavity or thin-wall cavity well slides. These beads were coated with streptavidin ($2a = 1250$ and $2a = 810$ nm) or anti-digoxigenin ($2a = 2120$ nm) and have been used previously in DNA-stretching work. Dimers were produced *in situ* by individually optically trapping each bead and “pressing” the beads together for around 10 s. Dimers' dynamics were examined in a 2 wt.% $M_n = 20000$ g/Mol PEG (Sigma-Aldrich) in aqueous [NaCl] = 10 mM solution (unless noted otherwise). The viscosity of the solution was measured at 13 mPa.s using conventional single-bead passive microrheology. This solution was chosen over water to slow the dimers' dynamics and to increase drag forces. Some salt was included to reduce electrostatic screening to improve adhesion between the beads. It was notable that these beads appeared to stick together more readily than uncoated beads, which were generally observed to require higher salt concentrations to adhere. Dimers were examined in either an “active” mode or “passive” mode. In the active mode, the motion of the dimer was monitored as a triangular displacement wave was applied to the slide via a piezo-stage (Physik Instrumente E-710-3CD):

$$y(t) = (A/\pi) \sin^{-1} [\sin(2\pi ft)], \quad (3)$$

where y is the stage displacement, A is the peak-to-peak amplitude, and f is the frequency, which produces an oscillating translational flow, of velocity v_y , at the trap:

$$v_y(t) = 2Af \operatorname{sgn} [\sin(2\pi ft)], \quad (4)$$

where sgn is the signum (or sign) function [20]. This flow is used to impart a constant positive or negative force to a trapped particle. In the “passive” mode, the restricted diffusion of the dimer was monitored. For the active measurements, laser power at the source was set to 2.0 W, frequency of oscillation was fixed at $f = 2$ Hz, and either the peak-to-peak amplitude or the position relative to the surface varied. For the passive measurements, the laser power was varied. For both active and passive measurements, the height of the optical trap Δz about the instrument's natural focus at $\Delta z = 0$ was varied.

3. RESULTS

Images of a dimer at six optical trap heights Δz in translational flow are illustrated in Fig. 1(A). Changing the height of the optical trap has a significant effect on the particle's image and could be expected to modify the image statistics. Positive and negative translational flow, corresponding to positive going or negative going displacements of the stage, produces subtle changes in the dimer's image—these changes suggest the dimer may be rotating in flow. Naively, it might be expected that the particle would simply translate in translational flow as is suggested in Fig. 1(Bi). However, this presupposes that the dimer is trapped at the point of contact between the beads. If this was not the case, rotation could be expected as illustrated in Fig. 1(Bii). The effective drag force on a bead increases as it approaches a surface, and this proximity effect might be expected to further modify the rotation of the dimer, as suggested by Figs. 1(Biii) and 1(Biv).

Acquired images, $I(x, y)$, were background corrected and background normalized:

$$I'(x, y) = [I(x, y) - I_0(x, y)]/\langle I_0 \rangle, \quad (5)$$

where $I_0(x, y)$ is a background image of the same region without the particle present. A typical background-corrected and -normalized image of a dimer is shown in Fig. 2(A) along with an associated line profile in Fig. 2(D). Image moments were computed according to

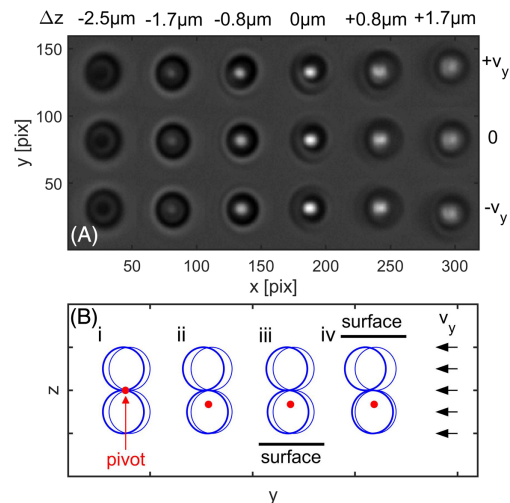


Fig. 1. (A) Images of a dimer in translational flow at six trap heights; $+v_y$ and $-v_y$ images are offset for clarity. (B) Sketch of movement expected in translational flow, with pivot location and proximity to surfaces.

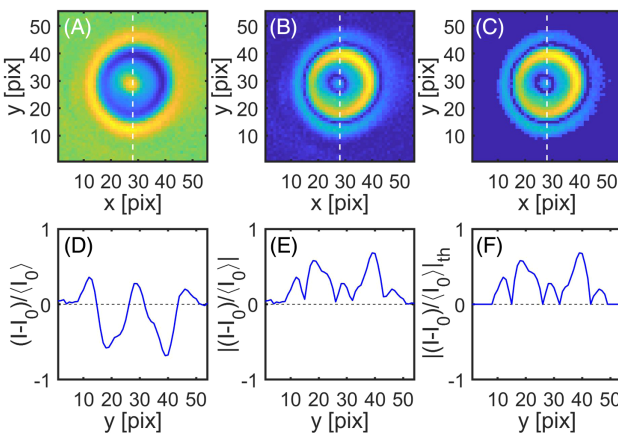


Fig. 2. (A) Background-corrected/normalized image of a dimer, I' , with (D) associated line profile. (B) Rectified background-corrected/normalized image $|I'|$ with (E) associated line profile. (C) Thresholded rectified background-corrected/normalized image $I'' = |I'|_{\text{thres}}$, with (F) associated line profile. See Data File 1 for underlying values.

$$M_{ij} = \sum_x \sum_y x^i y^j I''(x, y), \quad (6)$$

where I'' is the rectified and thresholded I' :

$$I''(x, y) = |[I(x, y) - I_0(x, y)]/\langle I_0 \rangle|_{\text{thres}} = |I'(x, y)|_{\text{thres}} \quad (7)$$

[21]. Rectification was used to ensure that the image intensity was nonnegative, and thresholding was used to suppress the effects of residual nonnegative shot noise on the moment calculation. Figures 2(B) and 2(C) [with associated line profiles in Figs. 2(E) and 2(F)] show the effect of rectification and thresholding on the image shown in Fig. 2(A). Central moments were computed according to

$$\mu_{pq} = \sum_x \sum_y (x - \bar{x})^p (y - \bar{y})^q I''(x, y), \quad (8)$$

where \bar{x} and \bar{y} are the image's center of mass defined as

$$\bar{x} = M_{10}/M_{00}, \quad (9)$$

$$\bar{y} = M_{01}/M_{00} \quad (10)$$

[21]. Note that the centers of mass are computed from the rectified/thresholded image I'' , and the central moments are computed from the unrectified/unthresholded image I' .

Translational flow for a triangular displacement wave with peak-to-peak amplitudes $A = 1, 2 \dots 7 \mu\text{m}$ and frequency $f = 2 \text{ Hz}$, resulting in flow rates of $v_y = 4, 8 \dots 28 \mu\text{m/s}$, were applied to optically trapped dimers and isolated $2a = 1250 \text{ nm}$ microspheres at an optical trap height $\Delta z = -0.8 \mu\text{m}$. Figure 3 shows the resulting normalized first moment (or center of mass) $\bar{y} = M_{01}/M_{00}$ and first central moment μ_{01} as the amplitude is stepped. For both the dimer and sphere, \bar{y} switches between more positive and more negative values about an equilibrium value, with a difference from equilibrium that increases with the amplitude of the applied triangular wave. As shown in Fig. 3(B), μ_{01} also switches between two values about an equilibrium value

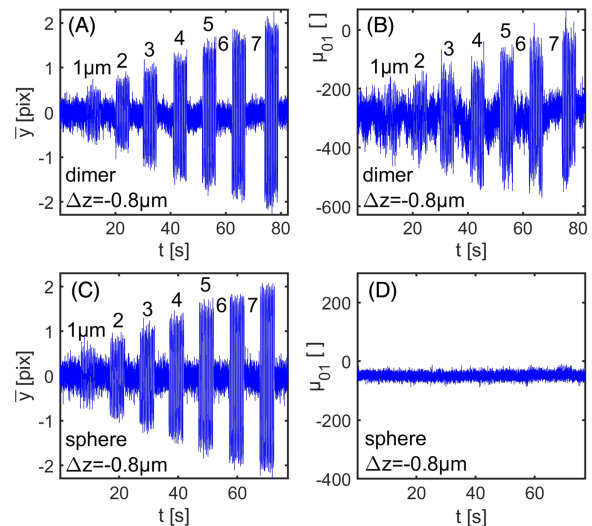


Fig. 3. (A) Center of mass and (B) central moment of a dimer in translational flow at trap height $\Delta z = -0.8 \mu\text{m}$ as velocity is stepped. (C) Center of mass and (D) central moment at trap height $\Delta z = -0.8 \mu\text{m}$ of an isolated sphere in translational flow as velocity is stepped. See Data File 2 for underlying values.

with a difference that (generally) increases with amplitude of the triangular wave. μ_{01} for the sphere does not vary with amplitude as shown in Fig. 3(D). The sphere is rotationally symmetric and its image will not change even if it rotates. The dimer is not rotationally symmetric, and rotation could be expected to affect the image and derived statistics, including μ_{01} , which is the lowest order central moment.

Figure 4(A) shows an expanded view of the behavior of μ_{01} during the $A = 6 \mu\text{m}$ triangular displacement cycle along with a fit. The oscillating section of the data was fitted to a function of the form

$$\mu_{01}(t) = u \text{smooth}[\text{sgn}(\sin[2\pi f(t - t_0)])] + u_0, \quad (11)$$

where u is an amplitude, and u_0 is an offset. The lag time t_0 was determined separately by fitting \bar{y} to a similar function. Displacements between the extreme equilibrium positions are not instantaneous, and some running average smoothing with a fixed window size was included to reflect a reorientation time. The equilibrium $\Delta\mu_{01}$ was evaluated at each amplitude step according to

$$\Delta\mu_{01}^+ = +u + u_0 - u_{\text{eq}}, \quad (12)$$

$$\Delta\mu_{01}^- = -u + u_0 - u_{\text{eq}}, \quad (13)$$

where u_{eq} is the average μ_{01} value in the adjacent non-oscillating section of the data; $\Delta\mu_{01}^+$ and $\Delta\mu_{01}^-$ correspond to the average positive and negative excursions of μ_{01} about the equilibrium value. Figure 4(B) shows the fitted equilibrium $\Delta\mu_{01}$ with fluid velocity v at the trap. $\Delta\mu_{01}$ is fairly linear over the range of velocities tested. Also included in this figure is separate equilibrium $\Delta\mu_{01}$ for a $\Delta z = +0.8 \mu\text{m}$ active measurement. This change in trap height considerably modifies the relationship between equilibrium $\Delta\mu_{01}$ and v , introducing nonlinearity. Changing the trap's height Δz does not affect the apparent

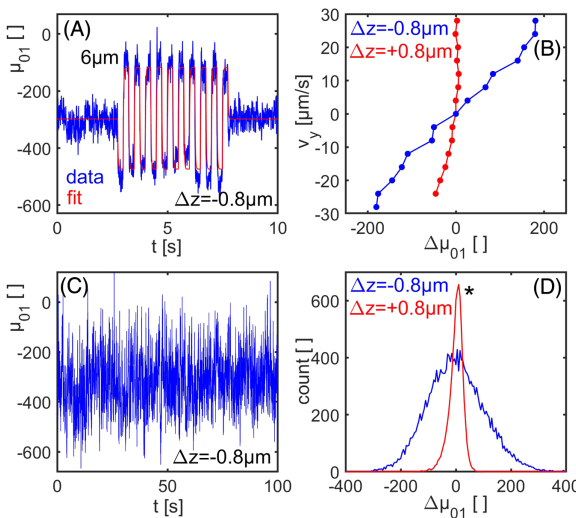


Fig. 4. (A) Active measurements with fit for a velocity of $\pm 24 \mu\text{m/s}$ at $\Delta z = -0.8 \mu\text{m}$. (B) Dependence of equilibrium active $\Delta\mu_{01}$ on velocity made at $\Delta z = -0.8$ and $\Delta z = +0.8$. (C) Passive measurements $\Delta z = -0.8 \mu\text{m}$. (D) Histogram of the passive $\Delta\mu_{01}$ at $\Delta z = -0.8$ and $\Delta z = +0.8$. For the $\Delta z = +0.8$ histogram, marked with an asterisk, the count is divided by three. See Data File 3 for underlying values.

behavior of a trapped sphere, suggesting that these changes are associated with changes in the image statistics and are not due to changes in the dimer's intrinsic dynamics. This observation was reinforced in a separate investigation in which an isolated sphere stuck to the upper surface of a thin cavity well slide was translated via the piezo-stage directly above a second optically trapped bead. Here, it was found that the resulting μ_{01} was quite sensitive to Δz and generally showed a nonlinear dependence on transverse displacement of the stuck bead. In addition to actively probing the relationship between translational flow and first central moment, the relationship was probed passively by monitoring the dimer's restricted diffusion in the trap. A typical restricted diffusion measurement for the dimer at $\Delta z = -0.8 \mu\text{m}$ is shown in Fig. 4(C). Deflections $\Delta\mu_{01}$ for the passive measurement were computed according to

$$\Delta\mu_{01} = \mu_{01} - \langle\mu_{01}\rangle_{\text{med}}, \quad (14)$$

where $\langle\mu_{01}\rangle_{\text{med}}$ is the median value, and a histogram of these data is shown in Fig. 4(D) along with a histogram for a passive measurement with the dimer at $\Delta z = +0.8 \mu\text{m}$. A median was used here to reduce sensitivity to non-Gaussian behavior. The histogram of the $\Delta z = -0.8 \mu\text{m}$ measurements are broad and Gaussian distributed, whereas the distribution for the $\Delta z = +0.8 \mu\text{m}$ measurements are much narrower and skewed.

The relationship between active and passive measurements is examined in Fig. 5 in more detail. For the active measurements, the equilibrium $\Delta\mu_{01}$ for a trapped dimer was measured as the velocity of the translational flow was stepped $v = \pm 4, \pm 8 \pm 12 \dots \pm 28 \mu\text{m/s}$ for optical trap heights $\Delta z = -2.5, -2.3, 2.1 \dots + 1.9 \mu\text{m}$ at a set laser power of $P = 2.0 \text{ W}$. For the passive measurements, the restricted diffusion of the same dimer was monitored over 100 s at a set laser power of $P = 0.25 \text{ W}$. All active and passive measurements are shown in Fig. 5 in blue, and model calculations are shown in

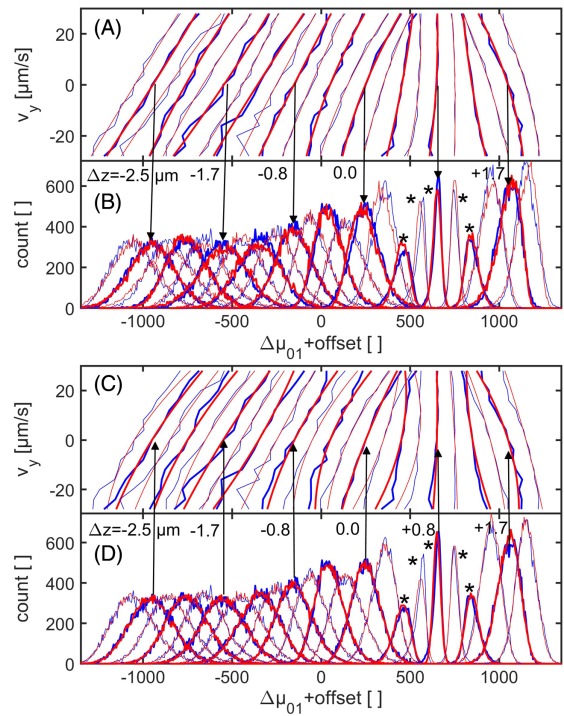


Fig. 5. (A), (C) Active and (B), (D) passive measurements (in blue) with fits (in red). For histograms marked with asterisks, the count is divided by three. See Data File 4 for underlying values.

red, with an offset for clarity. Figures 5(A) and 5(B) demonstrate that the passive measurements can be computed from the active behavior. Here, each active measurement shown in Fig. 5(A) was fitted to a function of the form

$$\Delta\mu_{01} = av + bv^2, \quad (15)$$

where a (units $[\mu\text{m/s}]^{-1}$) and b (units $[\mu\text{m/s}]^{-2}$) are fit coefficients. Passive measurements were computed assuming that

$$\Delta\mu_{01} = a(G(c)) + b(G(c))^2 + G(n), \quad (16)$$

where a and b are the fit coefficients above, $G(c)$ and $G(n)$ are 20 k random variables drawn from a Gaussian distribution with a standard deviation $\sigma = c$ or $\sigma = n$; histograms of the simulated $\Delta\mu_{01}$ are shown in Fig. 5(B). These simulated histograms agree well with those measured. c (units $[\mu\text{m/s}]$) and n (unitless) are constants chosen once for all calculations. c could be expected to depend on the relative trap stiffness between active and passive measurements (due to differences in laser power) and the location of the pivot. $G(n)$ is a noise term that was included to broaden the histogram. Without this noise, the computed histograms near the focus ($\Delta z = 0$) are much narrower than would otherwise be expected. Figures 5(C) and 5(D) demonstrate that the active measurement can be computed from the passive behavior. Passive measurements were computed assuming that

$$\Delta\mu_{01} = a'(G(1)) + b'(G(1))^2 + G(n), \quad (17)$$

where $a' = SD$ (unitless), $b' = 0.169 \times SD \times SK$ (unitless), and SD and SK are the measured long-time standard deviations and skewnesses, $G(1)$ and $G(n)$ are 20 k random variables

drawn from a Gaussian distribution with standard deviations $\sigma = 1$ or $\sigma = n$; histograms of simulated $\Delta\mu_{01}$ are shown in Fig. 5(D). These simulated histograms agree well with those measured. Active measurements were computed according to

$$\Delta\mu_{01} = a'(v/c) + b'(v/c)^2, \quad (18)$$

where a' and b' are the calculated coefficients described above. Agreement between the calculated and measured data is acceptable to good. Together, these results indicate that the relationship between passive and active measurements is well understood, and that active measurements, which probe the nonlinearity more directly but require access to a piezo-stage, are not strictly required.

In previous work [20], we examined the behavior of a microsphere in oscillating translational flow, and used these observations to map the restoring force of the optical trap in the xz plane. In that work, translational flow was used to impose a velocity v on the bead, which induced a drag force F producing a displacement Δx , which was the measured quantity. Assuming that the restoring force of the trap is proportional to displacement (that is, trap stiffness is constant), $v \propto F \propto \Delta x$ at equilibrium. By analogy, an imposed velocity on a dimer will induce a torque T and rotation $\Delta\theta$, implying that $v \propto T \propto \Delta\theta$ at equilibrium. It does not seem unreasonable that rotation of the dimer will modify $\Delta\mu_{01}$, and in many cases, we find that $v \propto \Delta\mu_{01}$, suggesting that $\Delta\mu_{01} \propto \Delta\theta$. In general, however, $\Delta\mu_{01}$ is not proportional to v . Following from Eq. (18), in the absence of noise, and assuming the nonlinearity can be approximated by a second order polynomial, $\Delta\mu_{01}$ can be expressed as

$$\Delta\mu_{01} = A\Delta\mu'_{01} + B\Delta\mu'^2_{01}, \quad (19)$$

where $A = a'/SD = 1$, and $B = b'/SD^2 = 0.169 \times SK/SD$, and where SD and SK are the measured long-time standard deviations and skewnesses of a passive measurement, which inform on the nonlinearity. $\Delta\mu_{01}$ is proportional to v [Eq. (18)] and therefore $\Delta\theta$, and can be determined by inverting this equation and choosing the appropriate root. In practice, it is usually simpler to avoid nonlinearity by choosing a height where the nonlinearity can be neglected, which here is off focus.

Based on the data shown in Fig. 5, at $\Delta z = -1.7 \mu\text{m}$, it could be expected that $\Delta\mu_{01}$ will be proportional to $\Delta\theta$. Passive measurements were acquired at four laser powers, mean-squared variation ($\langle\Delta\mu_{01}^2(t)\rangle$) computed, and these are shown in Fig. 6(A). Measurements at higher laser powers were acquired with a frame rate of 500 FPS, to better resolve short-time behavior. For free diffusion, it is expected that the rotational and translational mean-squared translational and rotational displacements (MSD) vary according to

$$\langle\Delta\theta^2(t)\rangle = 2D_\theta t, \quad (20)$$

$$\langle\Delta y^2(t)\rangle = 2D_y t, \quad (21)$$

where D_θ is the rotational diffusional coefficient about a short axis of the dimer, and D_y is the translational diffusion coefficient in the y direction [22,23]. Based on the equipartition theorem,

which asserts that each degree of freedom has on average $k_B T/2$ thermal energy, for diffusion restricted by the trap,

$$\langle\Delta\theta^2(t)\rangle = 2k_B T/k_\theta, \quad (22)$$

$$\langle\Delta y^2(t)\rangle = 2k_B T/k_y, \quad (23)$$

where k_B is Boltzmann's constant, T is temperature, k_θ is the effective trap stiffness for rotation θ about a short axis, and k_y is the trap stiffness for translation in the y direction. At shorter times, free diffusion will dominate, while at longer times, the restriction due to the trap dominates, and the MSD interpolates between these two regimes. If $\Delta\mu_{01}$ is proportional to $\Delta\theta$, then

$$\Delta\theta = h\Delta\mu_{01}, \quad (24)$$

$$\langle\Delta\theta^2(t)\rangle = h^2\langle\Delta\mu_{01}^2(t)\rangle, \quad (25)$$

where h is a unitless constant of proportionality or calibration constant. Based on Eqs. (25) and (20), it would be expected that $\langle\Delta\mu_{01}^2(t)\rangle \propto t$ at short times in the free diffusion regime. While the MSD $\langle\Delta\mu_{01}^2(t)\rangle$ do converge at short times, as expected, they do not converge to a line of slope one on the log-log plot. It can be easily demonstrated using Brownian dynamics that an incoherent noise source will introduce an offset to the MSD. As discussed previously, a source of noise is required to broaden the histograms to better match passive and active measurements. In Fig. 6(B), we subtract an offset from the MSD so that the short-time MSD is proportional to time. This offset is approximately equal to n^2 , to within a factor of two for all passive measurements shown in Fig. 5, and is assumed to be independent of laser power. To relate the $\Delta\mu_{01}$ to $\Delta\theta$, a calibration constant h is required. $\langle\Delta\theta^2(t)\rangle$ at short times can be computed if the diffusion constant D_θ is known. D_θ and D_y depend on the hydrodynamics of the dimer. We assume that we can represent this dimer, composed of a pair of $r = a = 1250/2 \text{ nm}$ radius beads, as a prolate ellipsoid with a short radius $r_s = a = 1250/2 \text{ nm}$ and a long radius $r_l = 2a = 1250 \text{ nm}$ and compute the rotational diffusion coefficient about the short axes to be $D_\theta = 0.0168 \text{ rad}^2/\text{s}$ and translational diffusion coefficient along the short axes to be $D_y = 1.91 \times 10^{-14} \text{ m}^2/\text{s}$ assuming a viscosity $\eta = 13 \text{ mPa}\cdot\text{s}$ and temperature $T = 293 \text{ K}$ [22,23]. With D_θ , h can be computed from the slope of the MSD at short times:

$$h^2 = \frac{1}{2D_\theta} / \frac{d}{dt} [\langle\Delta\mu_{01}^2(t)\rangle]_{t=0}. \quad (26)$$

For the data shown in Fig. 6(B), $h = 4.1 \times 10^{-4}$. h was determined here from a simultaneous best fit to the short-time MSD at all four laser powers to mitigate the effect of any uncertainty in the MSD offset. Figure 6(C) shows $\langle\Delta\theta^2(t)\rangle$ computed for this h , and Fig. 6(D) shows the associated $\langle\Delta y^2(t)\rangle$ along with the MSD calculated with the translational diffusion constant above. The measured and calculated translational MSD agree well at short times, and this agreement does suggest that representing the dimer as an ellipsoid is not unreasonable. With h determined, the trap stiffnesses k_θ and k_y can be determined at each laser power from the long-time behavior of the MSD.

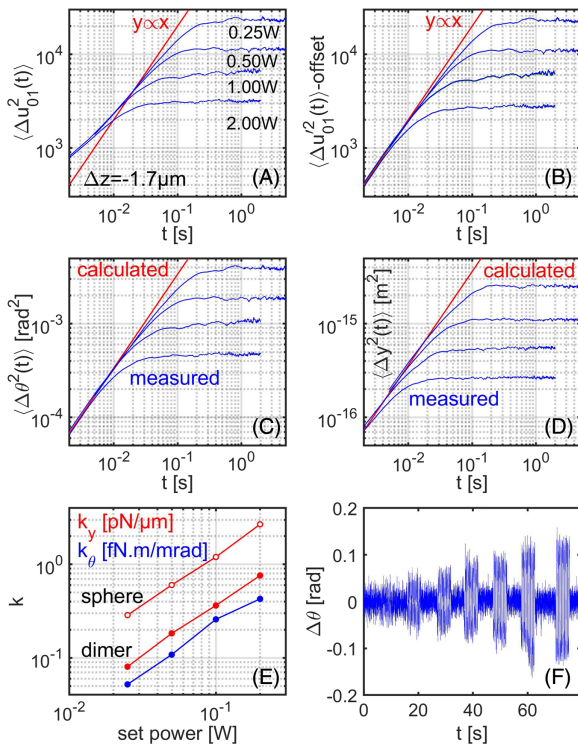


Fig. 6. (A) Measured mean-squared deflection $\langle \Delta\mu_0^2(t) \rangle$ at four laser powers (B) with offset correction for a dimer at trap height $\Delta z = -1.7 \mu\text{m}$. (C) Derived MSD's $\langle \Delta\theta^2(t) \rangle$ and associated $\langle \Delta y^2(t) \rangle$. (E) Rotational and translation trap stiffnesses for the dimer and for an isolated sphere. (F) Calibrated active measurement illustrating typical angular deflection. See Data File 5 for underlying values.

The calculated rotational and translational trap stiffness for the dimer and the translational trap stiffness for a $2a = 1250 \text{ nm}$ bead are shown in Fig. 6(E). All trap stiffnesses are proportional to the set laser power, with the translational trap stiffness for an isolated bead being a factor of three times greater than that of the dimer. We plot the associated calibrated active measurements for this dimer in Fig. 6(F) to illustrate the deflections that occur during translational flow. Here we see that the maximum angular displacement is around $\Delta\theta \approx 0.1 \text{ rad}$. Torque can be computed by multiplying the angular displacement by the trap stiffness, $T = k_\theta \Delta\theta$. For a $\Delta\theta = 0.1 \text{ rad}$ and a trap stiffness of $k_\theta = 4.2 \text{ fN.m/mrad}$, torque on the dimer is $T = 420 \text{ fN.m}$.

The torque transmitted to the dimer depends on the location of the pivot. According to Faxen's law, the drag force on a microsphere increases as it approaches a surface [24]. If we boldly assume that we can treat the two beads of the dimer as being hydrodynamically separate, then each bead will experience a different drag force as it approaches the surface, which could be expected to affect rotation. This situation is illustrated in Figs. 1(Biii) and 1(Biv). If the pivot is located below the point of contact between the beads, the dimer will rotate less near a surface below the dimer, and will rotate more near a surface above the dimer, in translational flow. To investigate, dimers were examined in oscillating translational flow as a surface was stepped towards the particle in 50 nm increments over 5–10 min. The distance between the dimer and surface was estimated by simultaneously imaging a reference bead that

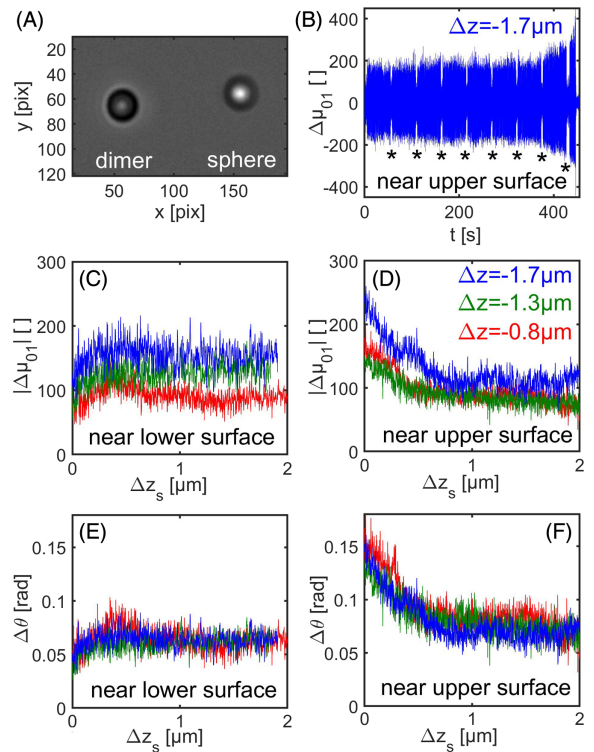


Fig. 7. (A) Image of an optically trapped dimer in translational flow near a surface with reference bead attached. (B) Measured $|\Delta\mu_{01}|$ in oscillating translational flow as the dimer is stepped towards the surface. Pauses are indicated with asterisks. $|\Delta\mu_{01}|$ as the dimer approaches (C) bottom surface and (D) top surface at three trap heights. Derived $|\Delta\theta_{01}|$ for the dimer as it approaches (E) bottom and (F) top surfaces. See Data File 6 for underlying values.

was stuck to the approaching surface. A typical image of the pair of particles near the top surface is shown in Fig. 7(A). Six dimers, at three trap heights, in a trap height range in which $\Delta\mu_{01} \propto \Delta\theta$, were examined. $\Delta\mu_{01}$ in one case is shown in Fig. 7(B). Intermittent pauses, marked with an asterisk in the figure, were included to determine the μ_{01} offset at equilibrium. $\Delta\mu_{01}$, at times when the flow direction is changing, and during the pauses were suppressed, and the data rectified; these rectified data $|\Delta\mu_{01}|$ are shown for the three trap heights near the lower surface in Fig. 7(C) and near the upper surface in Fig. 7(D) with Δz_s , which is the distance between the surface and first point of contact between surface and dimer. The $|\Delta\mu_{01}|$ data for $\Delta z = -1.3 \mu\text{m}$ and $\Delta z = -0.8 \mu\text{m}$ were scaled so that the average value $|\Delta\mu_{01}|$ for $\Delta z_s > 1.5 \mu\text{m}$ matched that of the $\Delta z = -1.7 \mu\text{m}$ measured, and the data were calibrated using the calibration constant determined earlier for the $\Delta z = -1.7 \mu\text{m}$ trap height. Calibrated $\Delta\theta$ for the measurements are shown in Figs. 7(E) and 7(F). As seen here, the rotation decreases near the lower surface and increases near the upper surface, as would be expected if the pivot about which the dimer turns is closer to the bottom of the dimer.

Active and passive measurements of the $2a = 810 \text{ nm}$ and $2a = 2120 \text{ nm}$ dimers were also examined. Because of low trap stiffnesses, the $2a = 2120 \text{ nm}$ dimers were studied in water. Active measurements are compared to the $2a = 1250 \text{ nm}$ dimer in Fig. 8. Included in each figure are the c values required to

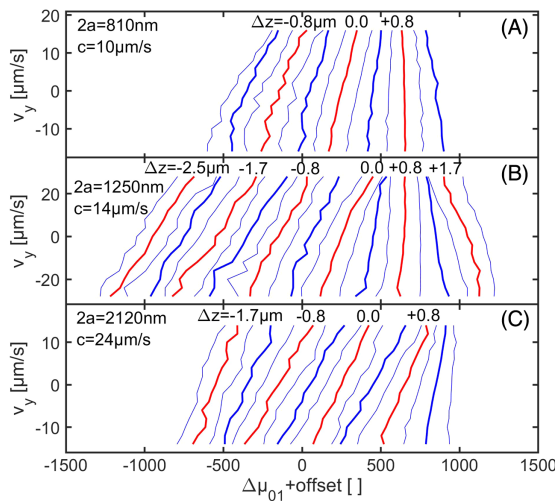


Fig. 8. Active measurements for (A) $2a = 810$ nm dimer ($\eta = 13$ mPa.s), (B) $2a = 1250$ nm dimer ($\eta = 13$ mPa.s), and (C) $2a = 2120$ nm dimer ($\eta = 1$ mPa.s). Red lines correspond to the Δz values indicated in figure and blue lines to intermediate values of Δz . See Data File 7 for underlying values.

model active and passive measurements. The c values differ between the beads and are proportional to the beads' sizes. It is expected that these values will depend on the trap stiffness ratio between active and passive measurements and the location of the pivot. The laser powers between active and passive measurements were fixed at 2.0 W/ 0.25 W = 8 in all cases. Generally, trap stiffness is proportional to laser power (as was demonstrated), indicating that the trap stiffness ratio between the pairs of beads is fixed, suggesting that the location of the pivot is changing between dimers. In Eq. (18), increasing c will reduce $\Delta\mu_{01}$ for a given v , suggesting that the pivot is shifting towards the point of contact between the beads as the bead size increases. Anecdotally (and perhaps surprisingly), the $2a = 2120$ nm dimer did appear, by eye, to translate more and rotate less in the translational flow.

4. DISCUSSION

It was demonstrated that the central moment of bright-field images of a near vertical optically trapped dimer in flow is, in general, nonlinearly related to fluid velocity and depends on the dimer's displacement from the image plane, and that this nonlinearity can be related to the restricted diffusion of the dimer, allowing the extraction of the underlying non-Gaussian statistics. While a correction for this nonlinearity is possible, it is simpler to minimize the nonlinearity by displacing the dimer to an off-focus position so that statistics are Gaussian. It was argued that in this linear range, the central moment is proportional to angular deflection $\Delta\theta = h\Delta\mu_{01}$. The constant of proportionality was computed by correcting the measured mean-squared variation $\langle\Delta\mu_{01}^2(t)\rangle$ for an offset, attributed to noise, and comparing the short-time behavior to the MSD $\langle\Delta\theta^2(t)\rangle$ predicted for an appropriately sized prolate ellipsoid. With h determined, the trap stiffness k_θ can be determined from the MSD at long times, and the torque on the dimer $T = k_\theta\Delta\theta$ can be estimated.

While only dimers were examined here, this approach may be useful for other axisymmetric particles, such as ellipsoids.

Attempts to probe the nonlinear relationship between $\Delta\theta$ and $\Delta\mu_{01}$ more directly were largely unsuccessful. As already noted, the central moment was monitored as a bead stuck to an upper surface in a thin wall cavity slide was translated over a second optically trapped bead. While this approach allowed independent positioning of the two beads and results supported the observation that the relationship between $\Delta\theta$ and $\Delta\mu_{01}$ was generally nonlinear, it was difficult to compare measurements directly to those measured for a dimer. This was mainly because it was difficult to repeatably set the separation between the beads to close to zero during translation, to replicate zero separation between the beads in the dimer, without the beads sticking together. It does appear to be possible to perturb the orientation of a trapped dimer with a second nearby trap. Understanding how this orientation relates to the positioning of the traps would appear to require a deep understanding of the trapping behavior of the dimer, which is beyond the scope of this paper. It is worth noting that we were unable to reorient a vertical dimer horizontally using a second trap on our system.

The origin of the small noise term required to broaden histograms in Figs. 5(B) and 5(D) and that produces an apparent offset in MSD in Fig. 6(B) is uncertain. Due to optical aberrations in the microscope and a slight misalignment of the trap, the image of the particle is not radially symmetric, and μ_{01} is non-zero, even when the dimer is nominally vertical; this non-zero offset can be observed for the dimer in Fig. 3(B) and for an isolated sphere in Fig. 3(D). This offset changes as the dimer is displaced in the z direction. An optically trapped particle undergoes restricted diffusion in the z direction, and therefore variation in the z position of a particle can potentially contribute to the measured $\Delta\mu_{01}$, producing uncorrelated noise.

The bright-field image of a spherical particle will exhibit radial symmetry, and consequently, the image's center of mass will reflect the location of the center of the particle in the transverse plane. A dimer is not spherical, and differences between the center of the dimer and the image center of mass could be expected as the particle rotates. These differences could be expected to depend on imaging conditions and image processing. Agreement between the free translational diffusion predicted and that observed suggest that perturbations to the center of mass by rotation are small in this study. If the relationship between the central moment and rotation can be understood, it does seem possible to correct the measured center of mass for rotation to estimate the particle's true center, if necessary.

The relationship among the transfer function, Gaussian distributed input, and output statistics, as described in Eq. (19), was determined empirically using simulation. This description, which connects standard deviation and skewness to an underlying nonlinearity, appears to be quite robust, as long as the transfer function is single valued over the range of interest. Equation (19) presumes that the underlying transfer function is described by a second order polynomial. If the transfer function is better approximated by a third order polynomial (and is single valued) then the relationship between the input (and presumed Gaussian distributed) μ'_{01} and output μ_{01} is

$$\Delta\mu_{01} = A\Delta\mu'_{01} + B\Delta\mu'^2_{01} + C\Delta\mu'^3_{01}, \quad (27)$$

where $A = a'/SD = 1$, and $B = b'/SD^2 = 0.169 \times SK/SD$, as before, and $C = 0.0407(KT - 1.32 \times SK^2)/SD^2$. KT is the measured kurtosis and is the fourth moment of the distribution over the standard deviation. To determine the input from the output, the roots of the cubic equation are required, and two roots must be discarded for physical reasons. This approach might be useful in other situations; for example, when nonlinearity is introduced by the electronics of the detection system. It is emphasized that this approach is appropriate only if the input statistics are Gaussian, which occurs when the restoring force is proportional to displacement; if the nonlinearity is introduced by the trap itself, this approach is not appropriate.

5. CONCLUSION

Optically trapped near vertical dimers were imaged in flow and at rest, and the dimer's image central moment was related to flow velocity and the at-rest restricted diffusion statistics. Angular deflections $\Delta\theta$ were computed from changes in the image central moment $\Delta\mu_{01}$, by modeling the dimer as a prolate ellipsoid and comparing short-time free diffusion behavior to compute the constant of proportionality b . With b determined, the angular trap stiffness can be estimated from the long-time restricted diffusion, and a torque, $T = k_\theta\Delta\theta$, on the dimer can be calculated.

Funding. Marsden Fund (MAU1810).

Acknowledgment. G. B. Jameson and M. A. K. Williams thank the Royal Society of New Zealand for funding.

Disclosures. The authors declare no conflicts of interest.

Data availability. Data underlying the results presented in this paper are available in Data Files 1–7, Refs. [25–31].

REFERENCES

1. S. Vivek and E. R. Weeks, "Decoupling of translational and rotational diffusion in quasi-2D colloidal fluids," *J. Chem. Phys.* **147**, 134502 (2017).
2. E. Sarmiento-Gómez, J. A. Rivera-Morán, and J. L. Arauz-Lara, "Single particle states of colloidal particles in 2D periodic potentials," *Soft Matter* **14**, 3684–3688 (2018).
3. L. Paterson, M. P. MacDonald, J. Arlt, W. Sibbett, P. E. Bryant, and K. Dholakia, "Controlled rotation of optically trapped microscopic particles," *Science* **292**, 912–914 (2001).
4. L. E. Altman, R. Quddus, F. C. Cheong, and D. G. Grier, "Holographic characterization and tracking of colloidal dimers in the effective-sphere approximation," *Soft Matter* **17**, 2695–2703 (2021).
5. C. van der Wel and D. J. Kraft, "Automated tracking of colloidal clusters with subpixel accuracy and precision," *J. Phys. Condens. Matter* **29**, 044001 (2017).
6. A. Ashkin, J. M. Dziedzic, J. E. Bjorkholm, and S. Chu, "Observation of a single-beam gradient force optical trap for dielectric particles," *Opt. Lett.* **11**, 288–290 (1986).
7. P. H. Jones, O. M. Marago, and G. Volpe, *Optical Tweezers: Principles and Applications* (Cambridge University, 2015).
8. S. Henderson, S. Mitchell, and P. Bartlett, "Direct measurements of colloidal friction coefficients," *Phys. Rev. E* **64**, 061403 (2001).
9. C. Gutsche, U. Keyser, K. Kegler, F. Kremer, and P. Linse, "Forces between single pairs of charged colloids in aqueous salt solutions," *Phys. Rev. E* **76**, 031403 (2007).
10. M. M. ElMahdy, C. Gutsche, and F. Kremer, "Forces within single pairs of charged colloids in aqueous solutions of ionic liquids as studied by optical tweezers," *J. Phys. Chem. C* **114**, 19452–19458 (2010).
11. A. Raudsepp, M. R. Griffiths, A. J. Sutherland-Smith, and M. A. K. Williams, "Developing a video tracking method to study interactions between close pairs of optically trapped particles in three dimensions," *Appl. Opt.* **54**, 9518–9527 (2015).
12. M. R. Griffiths, A. Raudsepp, and M. A. K. Williams, "Measuring the interaction between a pair of emulsion droplets using dual-trap optical tweezers," *RSC Adv.* **6**, 14538–14546 (2016).
13. M. D. Wang, H. Yin, R. Landick, J. Gelles, and S. M. Block, "Stretching DNA with optical tweezers," *Biophys. J.* **72**, 1335 (1997).
14. A. Farré, A. van der Horst, G. A. Blab, B. P. B. Downing, and N. R. Forde, "Stretching single DNA molecules to demonstrate high-force capabilities of holographic optical tweezers," *J. Biophoton.* **3**, 224–233 (2010).
15. D. delToro and D. E. Smith, "Accurate measurement of force and displacement with optical tweezers using DNA molecules as metrology standards," *Appl. Phys. Lett.* **104**, 143701 (2014).
16. S. Suei, A. Raudsepp, L. M. Kent, S. A. Keen, V. V. Filichev, and M. A. Williams, "DNA visualization in single molecule studies carried out with optical tweezers: Covalent versus non-covalent attachment of fluorophores," *Biochem. Biophys. Res. Commun.* **466**, 226–231 (2015).
17. A. Raudsepp, L. M. Kent, S. B. Hall, and M. A. Williams, "Overstretching partially alkyne functionalized DSDNA using near infrared optical tweezers," *Biochem. Biophys. Res. Commun.* **496**, 975–980 (2018).
18. S. Simpson and S. Hanna, "Optical trapping of dielectric ellipsoids," *Proc. SPIE* **7762**, 77621B (2010).
19. R. Bowman, G. Gibson, A. Linnenberger, D. Phillips, J. Grieve, D. Carberry, S. Serati, M. Miles, and M. Padgett, "Red tweezers: fast, customisable hologram generation for optical tweezers," *Comput. Phys. Commun.* **185**, 268–273 (2014).
20. A. Raudsepp, M. A. Williams, and S. B. Hall, "Multidimensional mapping of the restoring force of an optical trap using triangular wave flow," *J. Mod. Opt.* **63**, 2308–2314 (2016).
21. M. Pawlak, *Image Analysis by Moments: Reconstruction and Computational Aspects* (Oficyna Wydawnicza Politechniki Wrocławskiej, 2006).
22. Z. Zheng and Y. Han, "Self-diffusion in two-dimensional hard ellipsoid suspensions," *J. Chem. Phys.* **133**, 124509 (2010).
23. F. Perrin, "Mouvement brownien d'un ellipsoïde - i. dispersion diélectrique pour des molécules ellipsoïdales," *J. Phys. Radium* **5**, 497–511 (1934).
24. S. Kim and S. J. Karrila, *Microhydrodynamics: Principles and Selected Applications* (Dover, 2005).
25. A. Raudsepp, G. B. Jameson, and M. A. K. Williams, "Optically trapped dimer image analysis," figshare (2021), <https://doi.org/10.6084/m9.figshare.16850923>.
26. A. Raudsepp, G. B. Jameson, and M. A. K. Williams, "Typical COMs and central moments of an optically trapped dimer and microsphere in oscillating translational flow," figshare (2021), <https://doi.org/10.6084/m9.figshare.16850929>.
27. A. Raudsepp, G. B. Jameson, and M. A. K. Williams, "Comparing active and passive measurements for an optically trapped dimer," figshare (2021), <https://doi.org/10.6084/m9.figshare.16850932>.
28. A. Raudsepp, G. B. Jameson, and M. A. K. Williams, "Comparing active and passive measurements for an optically trapped dimer to model calculations," figshare (2021), <https://doi.org/10.6084/m9.figshare.16850935>.
29. A. Raudsepp, G. B. Jameson, and M. A. K. Williams, "Computing the translational and rotational MSD of an optically trapped dimer and microsphere," figshare (2021), <https://doi.org/10.6084/m9.figshare.16850944>.
30. A. Raudsepp, G. B. Jameson, and M. A. K. Williams, "Behavior of an optically trapped dimer near a surface," figshare (2021), <https://doi.org/10.6084/m9.figshare.16850953>.
31. A. Raudsepp, G. B. Jameson, and M. A. K. Williams, "Comparing active measurement for optically trapped dimers composed of microsphere with different diameters," figshare (2021), <https://doi.org/10.6084/m9.figshare.16850956>.